CHAPTER 6
CALCULATED EXAMPLES AND DISCUSSION

6.1 SUMMARY

In this chapter, with the aid of the proposed thrust failure mechanism, the safety factors of the failures discussed in Chapter 1 are calculated. These safety factors are compared with the safety factors calculated using the widely used program SLOPE/W and based on the limit equilibrium method of slices. The geotechnical parameters used in the calculations appear in Table 6.1 below.

Table 6.1 Rock properties

Rock properties	**Sandy overburden**	**Sandstone**	**Shale (normal to bedding)**	**Shale (parallel to bedding)**
1	2	3	4	5
Density, kg/m^3	1900	2600	2700	-
Shear modulus, GPa	1.6	5.2	2.3	-
Bulk modulus, GPa	2.6	5.9	4.5	-
Tensile strength, MPa	1	5.5	3.5	1
Cohesion, kPa	40	700	400	100
Friction angle, deg.	32	22	14	8
Layer thickness*, m	20	12	8	-

* Average layer thickness

6.2 EXAMPLE 1: PIT A-2 SLOPE FAILURE

Let us begin with the failure that took place in Pit A-2, referred to in Section 1.2.2. The highwall slope profile appears in Figure 1.9. Two FLAC models were prepared for the stress state calculation: the first model corresponds to virgin conditions, and the second to an excavated slope contour (53^0 slope angle). Spoil material is simulated with the aid of applied pressure of 0.30MPa, equal to approximately 20m spoil height and with a unit weight of $15kN/m^3$. The thin sections of the embedded shale layer were taken from the failed area and the critical tensile stress was calculated (as discussed in Chapter 4 and Appendix A1.2).

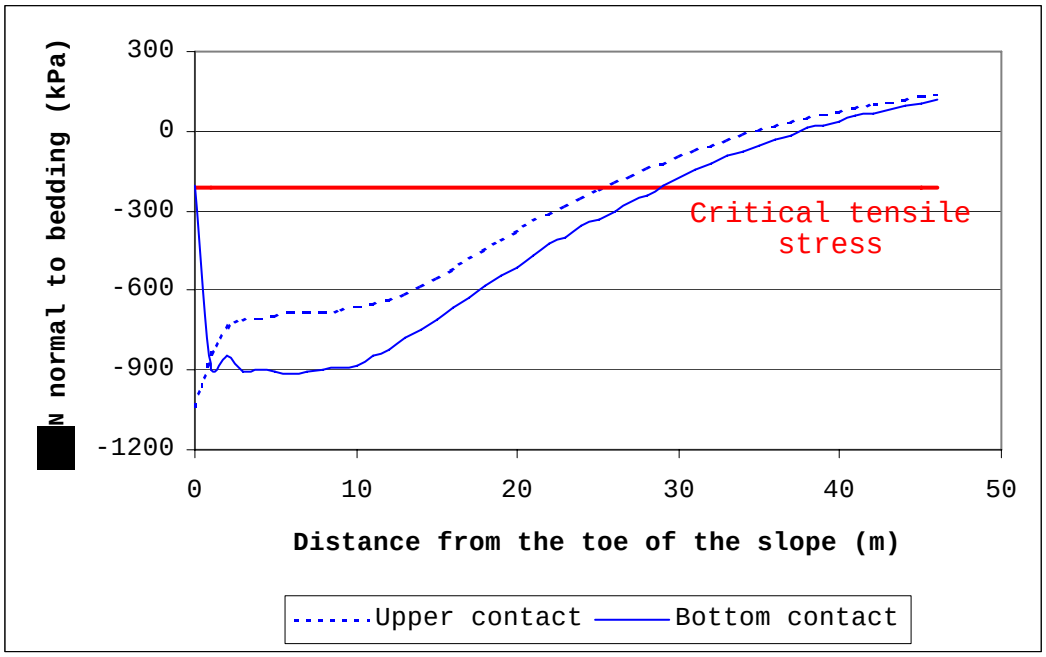

Figure 6.1

Stress component normal to bedding along the upper and bottom contact surfaces of the embedded shale layer with the value of the critical tensile stress, calculated in Chapter 4

Figure 6.1 shows the normal to bedding stress component along the upper and bottom contact surfaces of the embedded shale layer, together with the critical tensile stress $\Delta\sigma_N^P$. From the figure, the frictional zone length along the upper and bottom contact surfaces has values of 25m and 29m respectively.

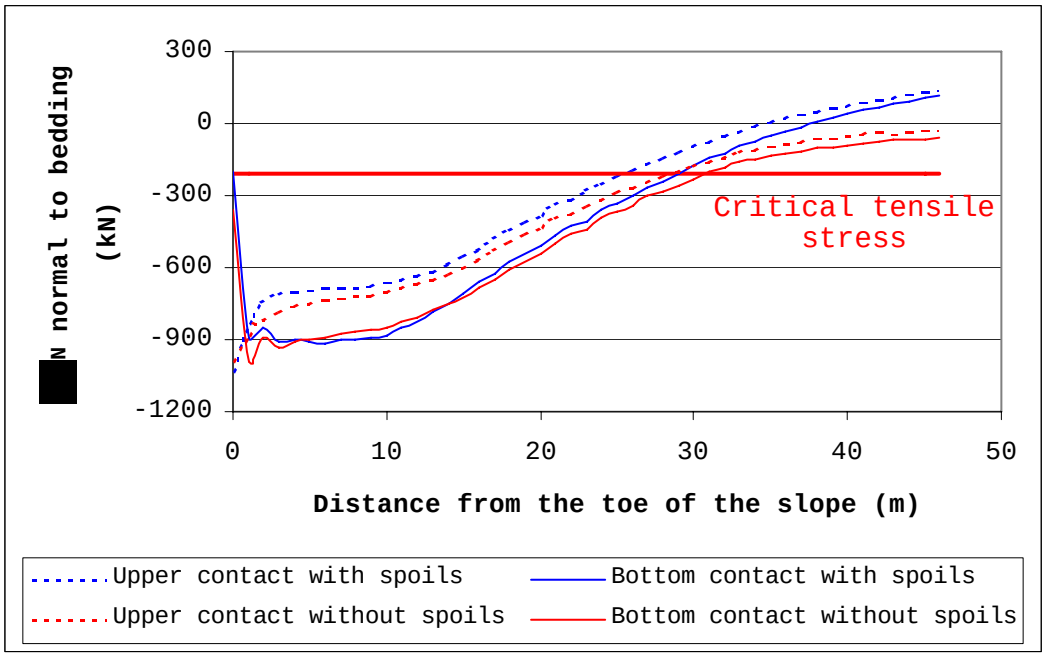

Figure 6.2

Stress component normal to bedding for the slope profile at Pit A-2 with and without spoils, together with the critical tensile stress $\Delta\sigma_N^P$

To determine the effect of the spoil pile, another FLAC model without spoils was run. Figure 6.2 presents the plot of the stresses normal to bedding (cases with and without spoils), together with the critical tensile stress $\Delta\sigma_N^P$. It can be seen that the tensile fracture at the contact increases in length from 25m to 28m and from 29m to 32m at the upper and the bottom contacts respectively, if there were no spoils dumped on the slope. Hence, we can conclude that spoils have an

anchoring effect on slope stability. However, this effect may not be strong enough to prevent failure as, at the same time, the spoil material increases the shear stress component along the active block shear failure surfaces.

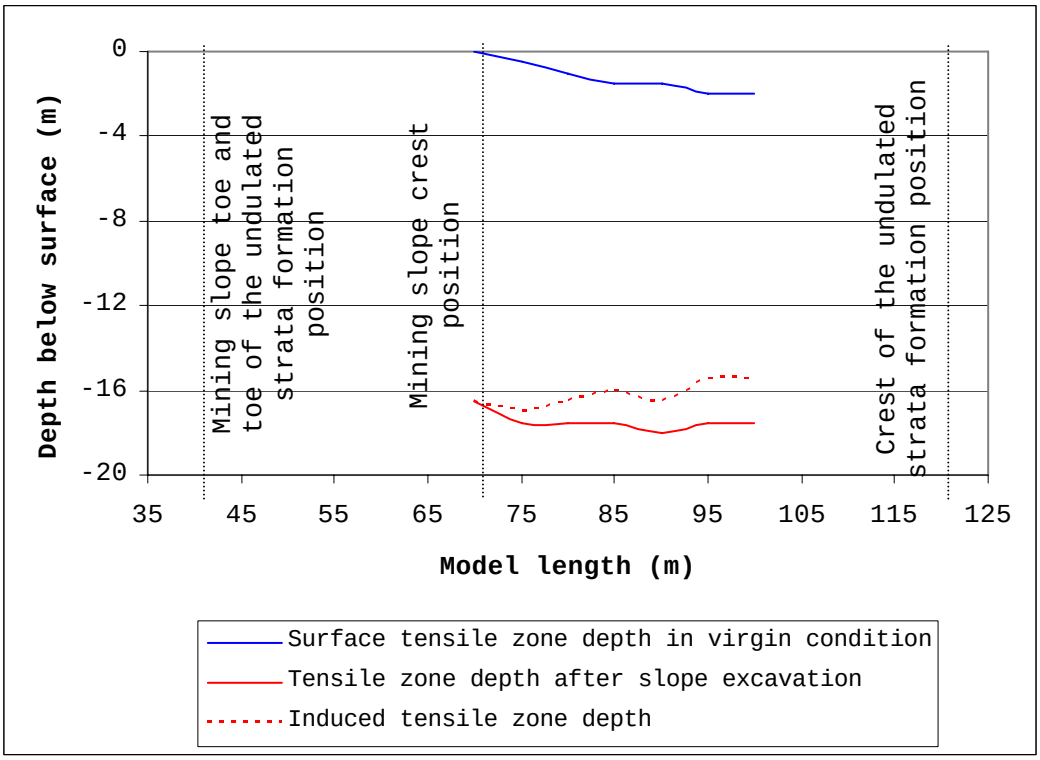

Figure 6.3

Tensile zone depth above the undulated strata formation in virgin conditions and after slope excavation

As was discussed in Section 3.6, there is a pre-existing tensile stress zone at the ground surface above the formation crest, which extension (in both directions: horizontal and vertical) is triggered by the mining activities. Therefore, the induced tensile horizontal stress zone depth we take for the contour of the surface vertical tensile fracture propagation. Figure 6.3 shows the depth of the tensile horizontal stress zone in virgin conditions and after slope

excavation. Their difference indicates the expected surface tensile fracture depth.

It is obvious that we could have two possible failures – along the upper and along the bottom contact surfaces (dash). This means that we have to calculate a safety factor along these two potential failure surfaces. The two possible scenarios with their active and passive blocks are shown in Figures 6.4a and 6.4b for upper and bottom contacts respectively. At the mine, the phreatic surface was measured to be 23m below surface, and this has been taken into account in the subsequent calculations, assuming a dry slope toe.

6.2.1 Example 1a: Safety factor calculations along the upper contact surface

Step 1. Average friction angle along the inner shear failure surface

With the aid of Equation 5.2, Figure 5.9 and Table 6.1 we calculate the average inner friction angle

$$\phi_{avI} = \boldsymbol{arctan}\frac{15.3\boldsymbol{tan}32 + 9.4\boldsymbol{tan}22}{24.7} = 28^0$$

Step 2. Inner shear surface inclination angle

Based on the arguments in Chapter 5, we assume an inner shear zone surface inclination angle of $\beta_I = 45^0$.

Step 3. Inner vertical tensile fracture

A vertical line is drawn from the crest of the slope to the zero horizontal stress contour.

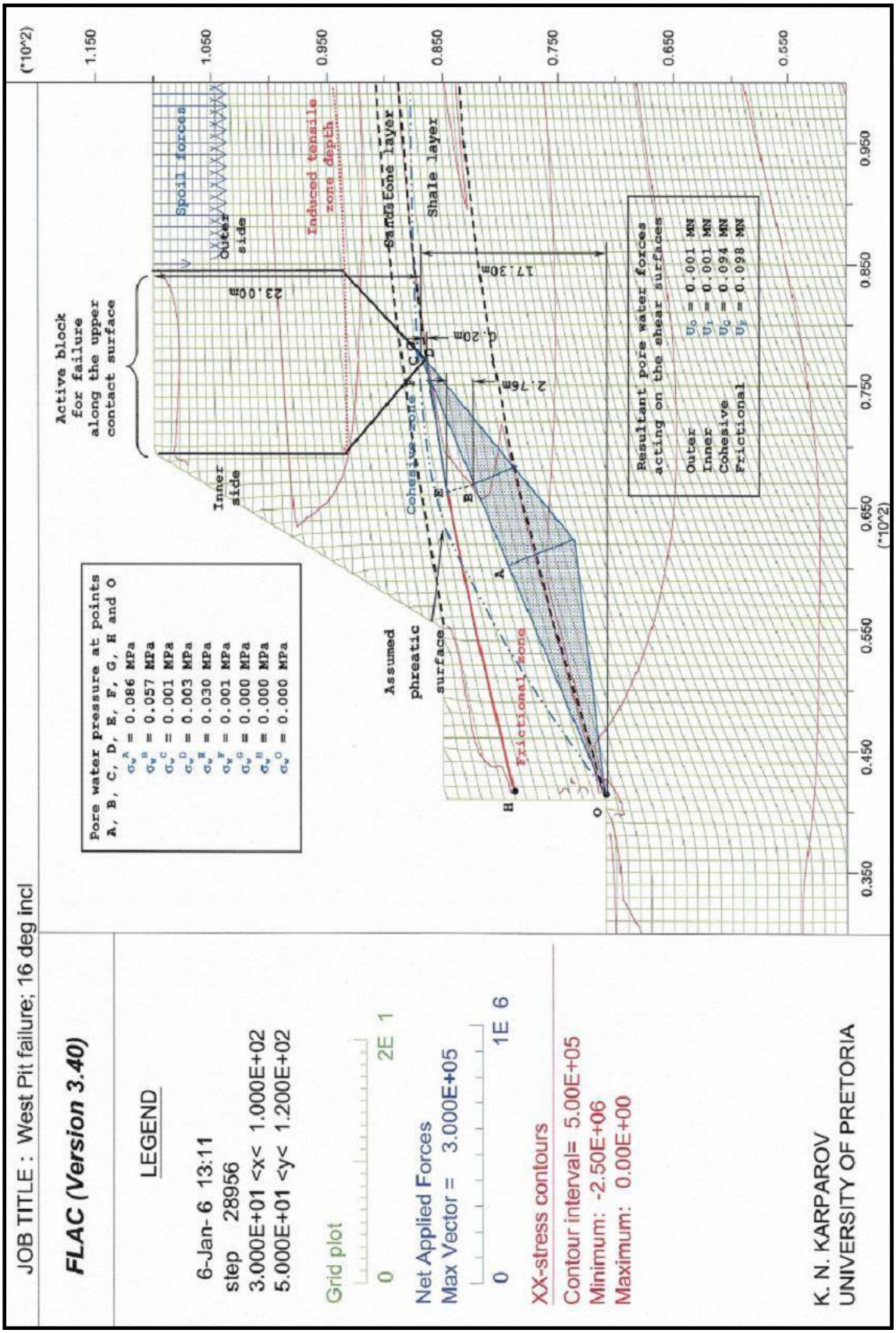

Figure 6.4a
Single slope profile along the upper contact in Colliery A-2 with tensile fractures along the upper contact surface of the embedded shale layer

Step 4. Inner shear failure surface

From the bottom end of the tensile fracture in the overburden to the upper contact surface of the embedded shale layer a line is drawn which dips toward the solid, with angle β_I=45° to the horizontal.

Step 5. Average cohesion of the inner shear failure surface

From Figure 6.4a, after Equation 5.3 and Table 6.1, the average cohesion along the inner shear failure surface:

$$c_{avI} = \frac{6.21*0.04 + 2.76*0.7}{8.97} = 0.243 \text{ MN/m}^2$$

Step 6. Inner shear failure surface length

The length of the shear zone surface is $l_I = \sqrt{2}\Delta h$, where Δh is the elevation difference between the base of the tensile zone and the top shale contact. Hence, l_I = 9.83m.

Step 7. Average friction angle along the outer shear failure surface

After Equation 5.2, Figure 5.9 and Table 6.1 we have:

$$\phi_{avO} = \arctan\frac{14.5\tan 32 + 8.5\tan 22}{23} = 29^0$$

Step 8. Outer shear surface inclination angle

As for the inner shear surface, we assume a 45° inclination, i.e. $\beta_O = 45^0$.

Step 9. Outer shear failure surface

From the intersection of the inner shear failure surface with the upper contact of the embedded shale

layer a line is drawn upwards and towards the solid, with angle β_O=45° to the horizontal, until the intersection with the bottom contour of the induced tensile zone in the overburden.

Step 10. Outer vertical tensile fracture

From the upper end of the outer shear failure surface a line is drawn vertically upwards to surface.

Step 11. Average cohesion of the outer shear failure surface

After Equation 5.3, Figure 6.4a and Table 6.1 for the average cohesion along the outer shear failure surface, we have:

$$c_{avO} = \frac{6.04*0.04 + 2.93*0.7}{8.97} = 0.256\ MPa$$

Step 12. Outer shear failure surface length

The length of the outer shear zone surface is $l_O = \sqrt{2}\Delta h$, where Δh is the elevation difference between the base of the outer tensile zone and the top shale contact. Hence, l_I = 9.24m

Step 13. Frictional zone load

From Equation 5.4, Table 6.1 and Figure 6.4a we calculate the frictional zone load P_f = 4.194 MN/m^2

Step 14. Frictional zone length

From Figure 6.1 we have l_F = 25m frictional zone length, which is plotted in Figure 6.4.

Step 15. Average angle at the frictional zone failure surface

From Figure 6.4a we have an average $\varpi_F = 13^0$ inclination of the frictional zone failure surface.

Step 16. Cohesive zone load

From Equation 5.4, Table 6.1 and Figure 6.4a we calculate the frictional zone load P_c = 2.223 MN/m^2

Step 17. Cohesive zone length

From Figure 6.4a we have l_c = 11m in length after construction of the active block.

Step 18. Average angle at the cohesive zone failure surface

From Figure 6.4a we have an average $\varpi_C = 10^0$ inclination of the frictional zone failure surface.

Step 19. Active block load calculation

After Equation 5.4, Table 6.1 and Figure 6.4a we have P_A = 5.365 *MN*.

Step 20. Angle at the active block wedge

From Figure 6.4a we have $\varpi_A = 9^0$.

Step 21. Passive block reaction force to the inner failure surface

The passive block driving and resisting forces are the sum of respectively driving and resisting forces of the frictional and cohesive zones along the surface of the investigated failure. For the calculation of the driving and resisting forces along the frictional zone we use Equations 5.5b and 5.6 respectively, and for the

calculation of the driving and resisting forces along the cohesive zone we use Equations 5.7b and 5.7a respectively. Hence, after Equation 5.28 we have:

$$P_F^{dr} = P_F \sin \varpi_F = 4.194 \sin 13 = 0.943\ MN$$

$$P_F^{res} = P_F \cos \varpi_F \tan \phi_E = 4.194 \cos 13 \tan 8 = 0.574\ MN$$

$$P_C^{dr} = P_C \sin \varpi_C = 2.223 \sin 10 = 0.386\ MN$$

$$P_C^{res} = c_B l_B + P_C \cos \varpi_C \tan \phi_E = 11 * 0.1 + 2.223 \cos 10 \tan 8 = 1.408\ MN$$

Therefore, the total driving and resisting forces have values $P_P^{dr} = 1.329\ MN$ and $P_P^{res} = 1.982 MN$. Then the net passive block reaction force is $R_P = 0.653 MN$ (Equation 5.28) and this force in an opposite way acts to the active block load reaction (Figure 5.18b).

Step 22. Pore-water pressure calculations

Figure 6.4a shows a pore-water stress diagram and the calculated pore-water pressure at the points along the failure surfaces. From the figure we measure distances between the points GD, FD, DE and EH and their lengths are l_{GD}=1.18m, l_{FD}=1.18m, l_{DE}=2.65m and l_{EH}=11.19m respectively. Then using Equations 5.24 – 5.27 we calculate the resultant forces along the outer, inner, cohesive and frictional failure surface, which have following values:

$$U_O = \frac{l_{GD}\sigma_w^D}{2} = \frac{1.18 x 0.001}{2} \cong 0.001\ MN$$

$$U_I = \frac{l_{FD}\sigma_w^D}{2} = \frac{1.18 x 0.001}{2} \cong 0.001\ MN$$

$$U_C = \frac{l_{DE}\left(\sigma_w^D + \sigma_w^E\right)}{2} = \frac{2.65(0.001 + 0.034)}{2} \cong 0.046\ MN$$

$$U_F = \frac{l_{EH}\sigma_w^D}{2} = \frac{11.19\,x\,0.034}{2} \cong 0.190\ MN$$

In Figure 6.4a the magnitudes of the resultant forces acting on the shear failure planes are also shown. It can be seen that the applied pore-water pressure diagram is different from the diagram in Figure 6.4a, which represents a general scenario and could appear in other geotechnical profiles.

Step 23. Condition for the existence of the inner shear failure surface

At the active block wedge we have a layer inclination angle $\varpi_A = 9^0$. After Equation 5.32 we have:

$$\eta = FOS_I = \frac{0.243 * 9.83 - 0.001\,tan\,28}{\frac{5.365(1 + sin\,9)\,sin\,45}{2} - 0.653\,sin\,28} = 1.266$$

With this value of the criterion η we do not have conditions for the inner shear failure surface formation to be created at the active block. This value is higher than that accepted by the author (1.3 for the minimum safety factor value), which is based on the safety factor coefficients for the open pit mines in other leading mining countries such as USA and Canada, as shown in Appendix 5

Step 24. Calculation of the reaction force acting along the outer shear failure surface

Following Equation 5.33 we have:

$$\overline{R} = \frac{5.365}{2}(1+\sin 9)\cos 45 - 0.653\cos 28 = 1.617\ MN$$

Step 25. Calculation of the outer shear failure surface safety factor

The outer shear failure surface will have a factor of safety equal to (Equation 5.35):

$$FOS_o = \frac{0.256*9.24 + \left[\frac{5.365}{2}(1-\sin 9)\cos 45 - 0.001 - 0*\sin 45\right]\tan 29}{1.617 + \frac{5.365}{2}(1-\sin 9)\sin 45 + 0*\cos 45} = 1.011$$

Step 26. Calculation of the safety factor on the basal shear failure surface

After Equation 5.36 for the base of the passive block we have a safety factor equal to:

$$FOS_B = \frac{4.194\cos 13\tan 8 + 11*0.1 + 2.223\cos 10\tan 8 - (0.094+0.098)\tan 8}{4.194\sin 13 + 2.223\sin 10} = 1.470$$

Step 27. Calculation of the slope stability factor of safety

After Equation 5.37 for the total slope stability factor of safety we have:

$$FOS = \frac{1.266*9.83 + 1.011*9.24 + 1.470*36.00}{9.83 + 9.24 + 36.00} = 1.375.$$

Therefore, the failure along the top contact will not occur.

6.2.2 Example 1b: Safety factor calculations along the bottom contact surface

Figure 6.4b shows the investigated slope profile with failure surface along the bottom contact and the pore-water pressure diagram. In Section 6.2.1 the calculation sequence of the proposed method was demonstrated. For simplicity, in this example, we will discuss only the results, as the calculation sequence itself is tabulated in Table A4.1 (Appendix 4).

As safety factors we have following values:

- FOS of the inner shear failure surface 0.914
- FOS of the outer shear failure surface 0.709
- FOS of the basal shear failure surface 0.750
- FOS of the slope 0.777

In this example we have safety factors 0.914 and 0.709 for the inner and outer shear failure surfaces respectively. Therefore, we have conditions for blocky-type of failure through the thrust failure mechanism.

In the case without spoils, safety factors along the failure surfaces have following values:

- FOS of the inner shear failure surface 1.031
- FOS of the outer shear failure surface 0.875
- FOS of the basal shear failure surface 0.663
- FOS of the slope 0.794

The above results show that we will have failure even in the case without spoils.

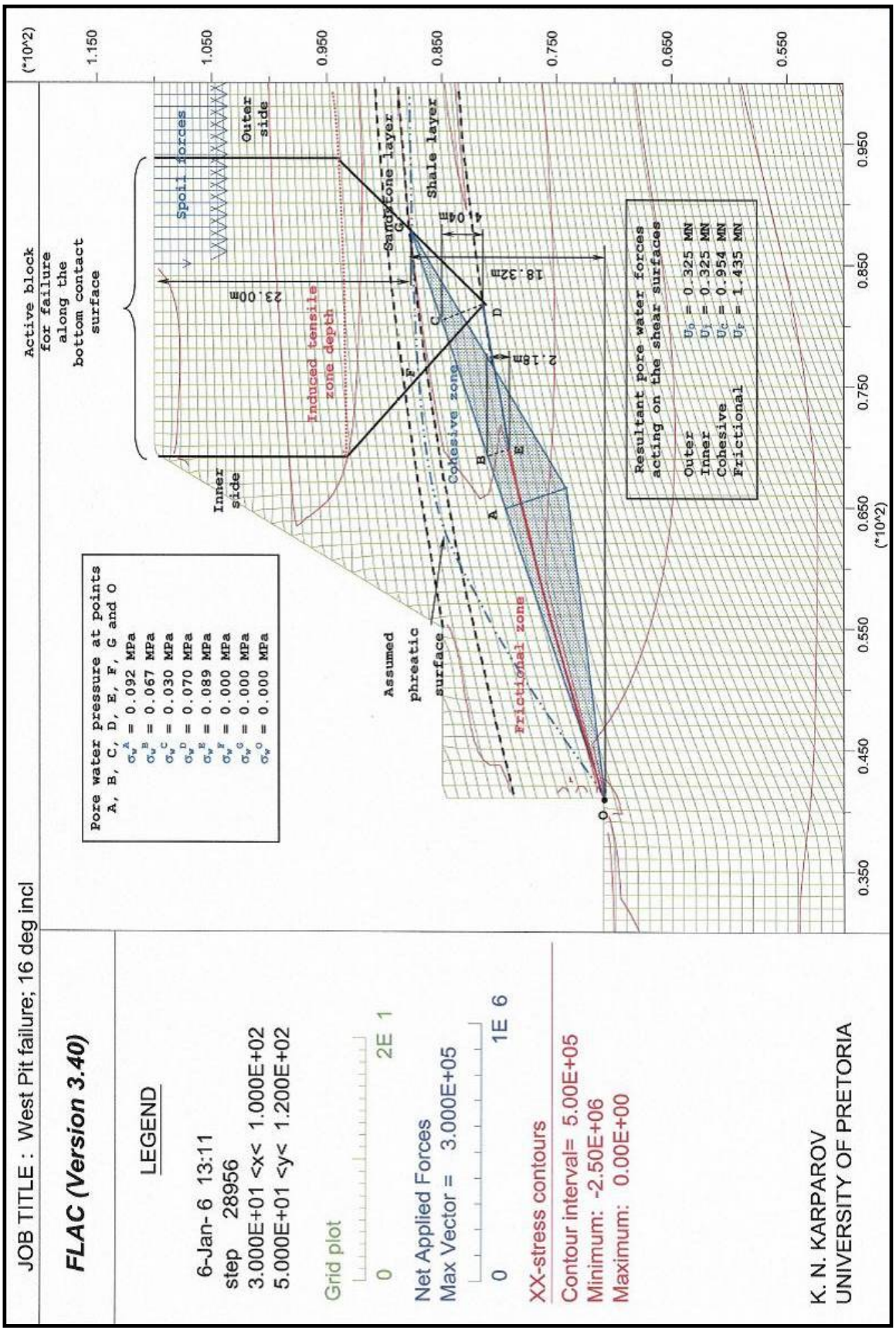

Figure 6.4b
Single slope profile along the upper contact in Colliery A-2 with tensile fractures along the bottom contact surface of the embedded shale layer

6.3 EXAMPLE 2: PIT A-1 SLOPE FAILURE

In Chapter 1 it was mentioned that the slope failure at pit A-1 took place in two stages: first, initial failure (circular type) in the sandy overburden; and a major collapse shortly after the cleaning operations. It is matter of interest what safety factor values for both failures we should have after the application of the proposed method.

The slope profile before failure appears in Figure 1.5. Three FLAC models were prepared for an investigation of the failure sequence. The first model presents the virgin mining conditions. The second model incorporates the slope with a slope angle 55^0 and presents the situation before initial failure (Figure 6.5). The third model (Figure 6.6) has a slope angle of 50^0 and corresponds to the highwall profile after the cleaning operations. From the models, stress differences normal to bedding ($\Delta\sigma_N$) along the top and the bottom contact of the embedded shale layer were calculated (Figure 6.7).

The slope failure took place in the same colliery as the failure discussed as Example 1, but in a mined out area. For this reason, it was impossible to prepare thin sections to study the micromechanical reasons for failure. The author assumes that the shale layer in the failed area had the same matrix and minerals as those for the failure shown in Section 6.2, Example 1. Therefore, we assume the same average carbon flake size and distribution and, consequently, the same calculated critical tensile stress (discussed in Chapter 4).

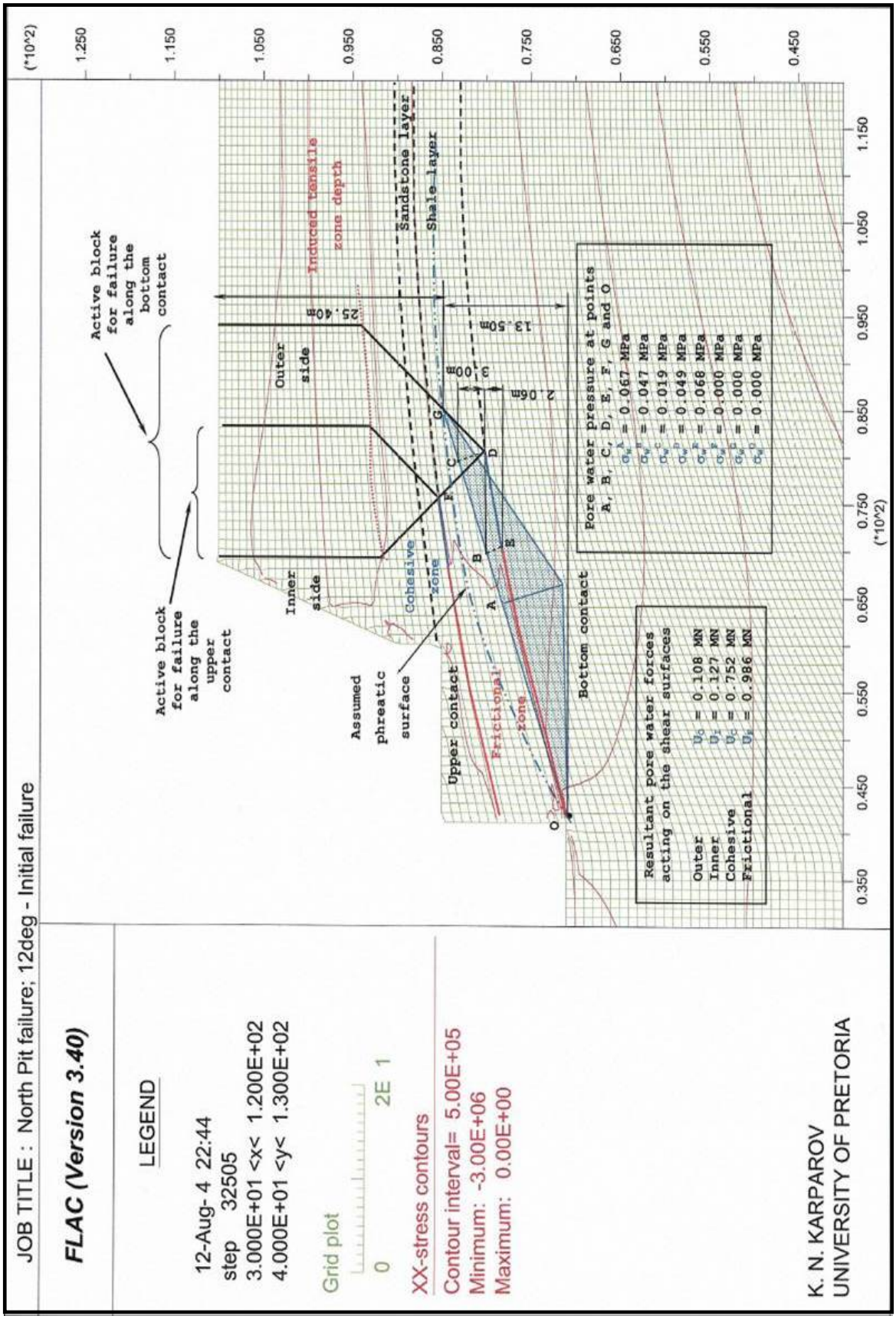

Figure 6.5
Failed slope profile in Colliery A-1 with the tensile fractures along the contact surfaces of the embedded shale layer before initial failure

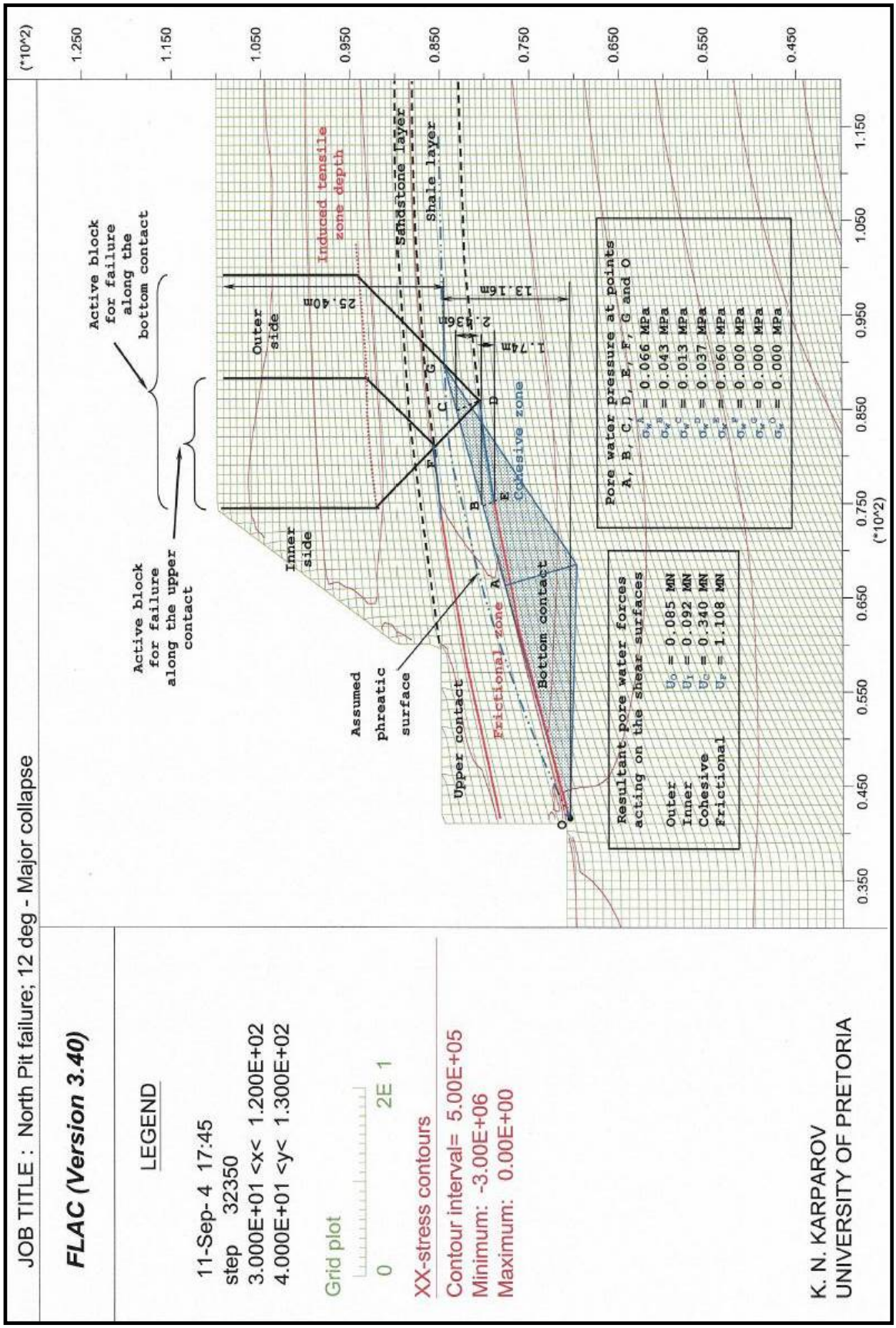

Figure 6.6
Failed slope profile in Colliery A-1 with the tensile fractures along the contact surfaces of the embedded shale layer before major collapse

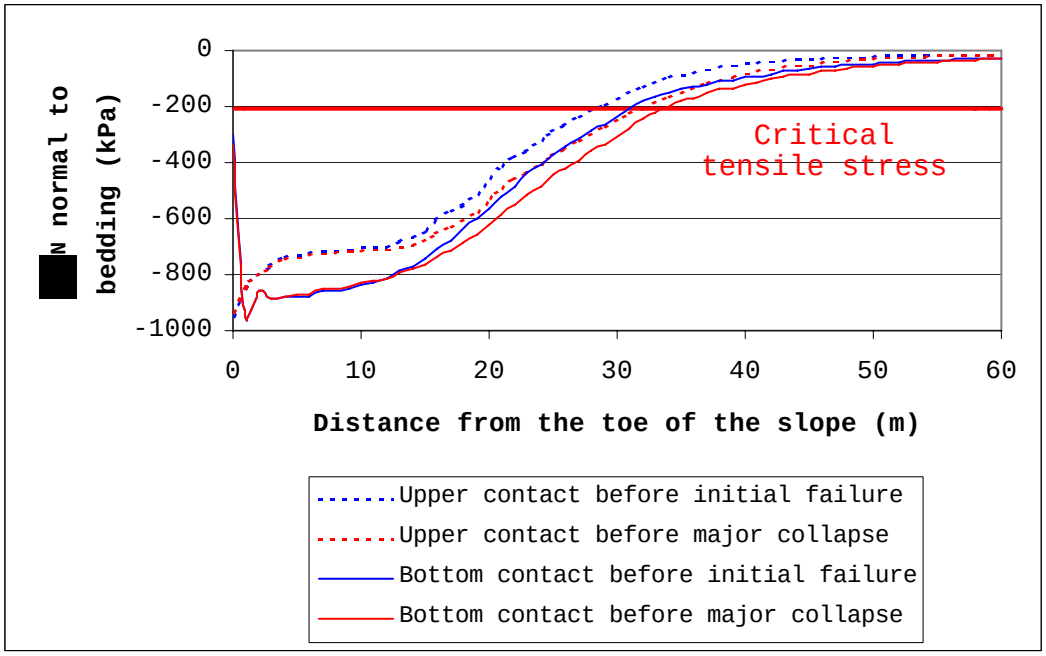

Figure 6.7
Stress component normal to bedding at the upper and bottom contact surfaces of the embedded shale layer with the value of the critical tensile stress, calculated in Chapter 4

Hence, in the figure we can plot the same σ_N^P value as calculated in Chapter 4 (the bold red line in Figure 6.7). It is seen that, because of the relaxation that result from cleaning operations, the tensile fracture increases from 27m to 32m from the toe of the slope along the upper contact and from 29m to 34m along the bottom contact. In this example, with the aid of the proposed method, we will calculate the safety factors of the two consequent failures at pit A-1, as discussed in Chapter 1. The calculated sequence and results are shown in Tables A4.2-A4.5 (Appendix 4). Shown here are only the safety factors of the separate surfaces and the slope safety factor.

According to the data recorded in the mining files, phreatic surface of the underground water was estimated at 25.40m below surface. From Figures 6.5 and 6.6 it can be seen that the upper contact surface of the embedded shale layer is above the estimated phreatic surface. Therefore, the pore-water pressure influence on the slope stability calculations is not taken into account.

Similar to the previous failure, the induced surface tensile zone was calculated and plotted in Figure 6.8. These induced tensile zones can be seen on a bigger scale plotted in Figures 6.5 and 6.6, for the profiles before the initial failure and before the major collapse.

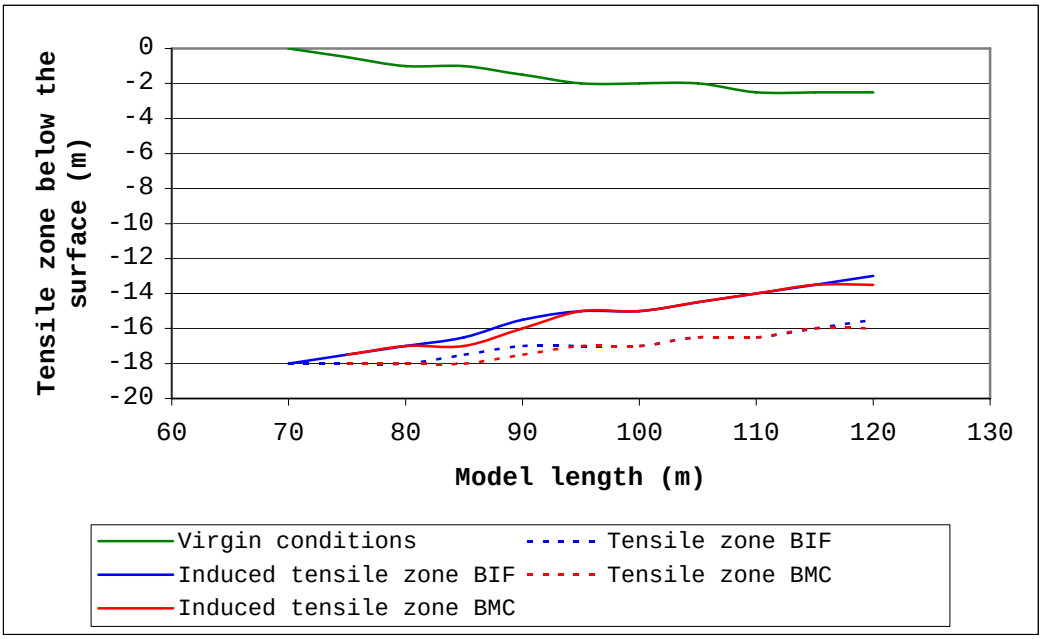

Figure 6.8

Tensile zone depth in virgin conditions, before the initial failure (BIF) and before the major collapse (BMC)

Calculated safety factors of the profile before initial failure:

At the upper contact,

- FOS of the inner shear failure surface 1.010
- FOS of the outer shear failure surface 0.955
- FOS of the basal shear failure surface 1.108
- FOS of the slope 1.062

At the bottom contact,

- FOS of the inner shear failure surface 1.036
- FOS of the outer shear failure surface 0.926
- FOS of the basal shear failure surface 0.833
- FOS of the slope 0.902

Calculated safety factors of the profile before major collapse:

At the upper contact,

- FOS of the inner shear failure surface 1.149
- FOS of the outer shear failure surface 0.935
- FOS of the basal shear failure surface 1.318
- FOS of the slope 1.224

At the bottom contact,

- FOS of the inner shear failure surface 1.161
- FOS of the outer shear failure surface 0.884
- FOS of the basal shear failure surface 0.826
- FOS of the slope 0.908

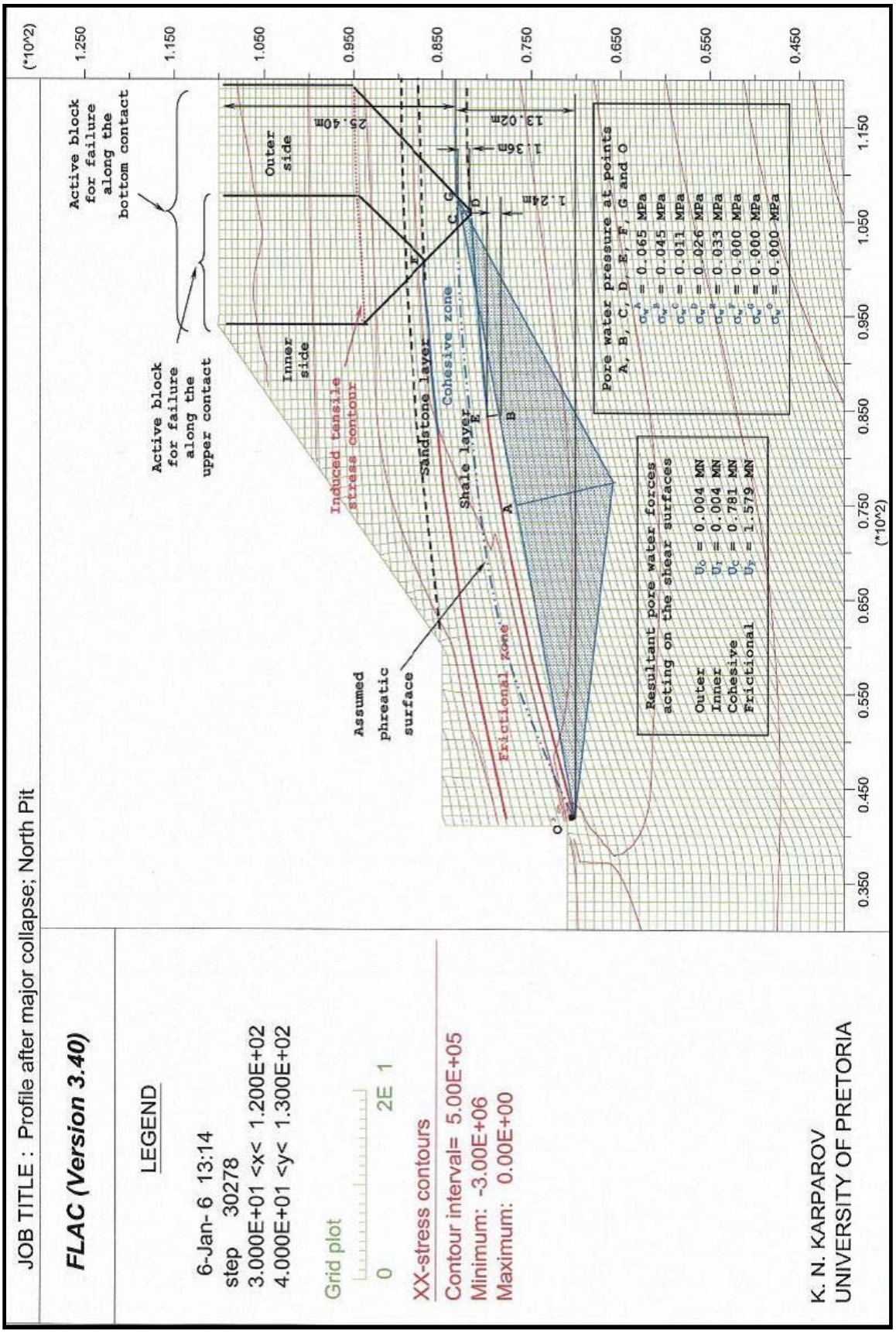

Figure 6.9
Profile after major collapse in Colliery A-1 with the tensile fractures along the contact surfaces of the embedded shale layer

From Figure 6.7 and the relatively lower safety factor along the bottom shale contact with the middle coal seam one might deduce the slope will always fail when the slope angle is reduced. Of course, this is not true and to confirm it let us reduce the slope angle of the profile from Figure 6.6 (slope before major collapse) to 37^0, which is the slope angle of the profile after the major collapse (see also Figure 1.4). This profile is shown in Figure 6.9.

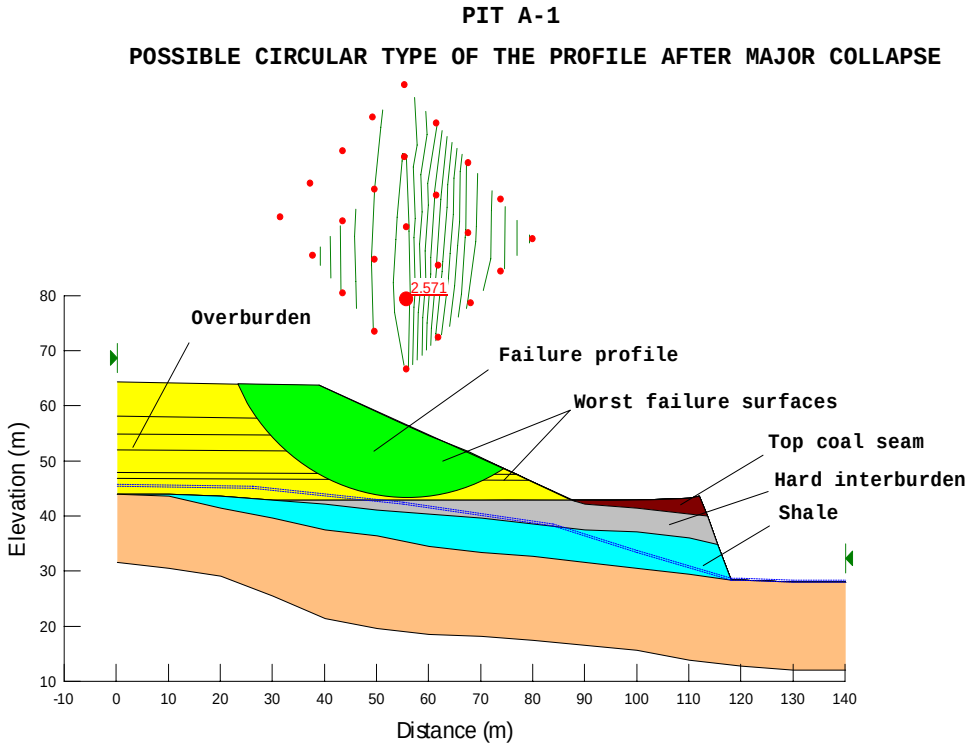

Figure 6.10

Safety factor for circular failure of the profile after major collapse after Morgenstern-Price

Figure 6.10 presents the profile after major collapse with the Morgenstern-Price method for the safety factor calculation. The other slope stability methods show similar values (ordinary – 2.206; Bishop – 2.575; Janbu – 2.164). The same model was run with FLAC and the stress difference normal to the bedding is plotted in

Figure 6.11. For the sake of comparison the stress normal to bedding ($\Delta\sigma_N$) in the contact surfaces from the profile before major collapse (Figure 6.7) and the critical stress ($\Delta\sigma_N^P$) are also plotted. Safety factor calculations are tabulated in Tables A4.6 and A4.7 (Appendix 4).

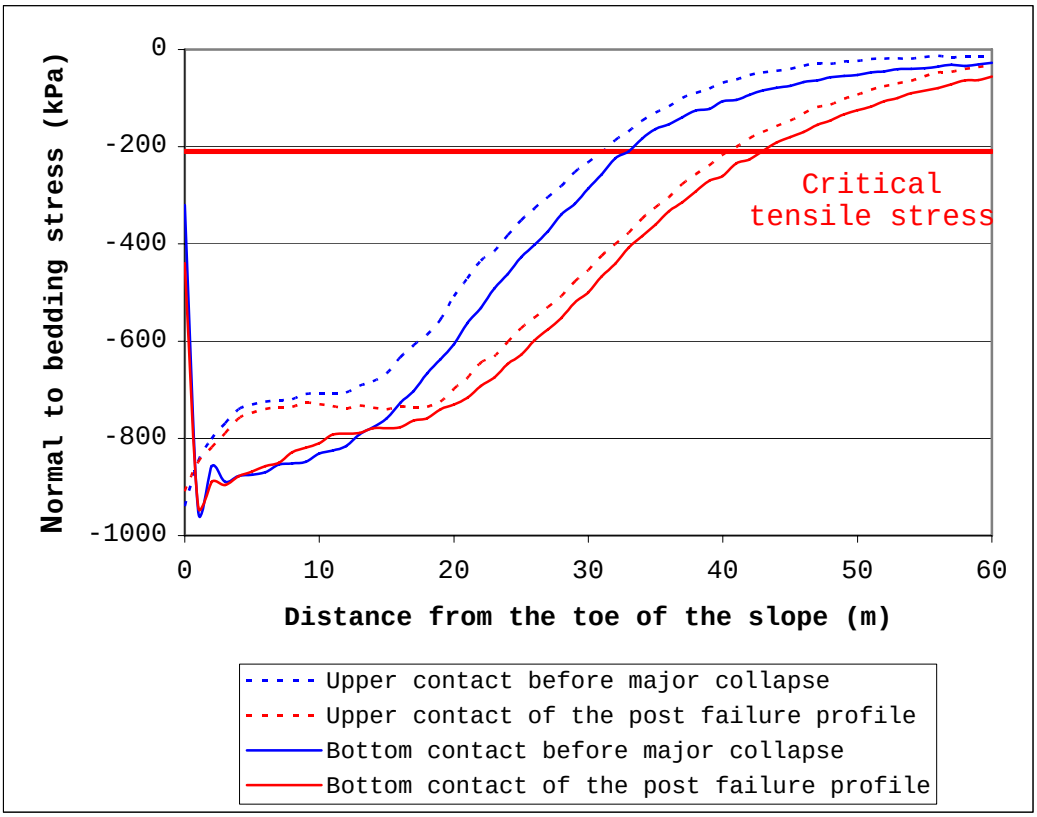

Figure 6.11

Stress component normal to bedding for the slope profile at Pit A-1 for the major collapse and the profile after major collapse

Calculated safety factors of the profile after major collapse:

At the upper contact,

- FOS of the inner shear failure surface 1.710
- FOS of the outer shear failure surface 1.222
- FOS of the basal shear failure surface 2.029
- FOS of the slope 1.860

At the bottom contact,

- FOS of the inner shear failure surface 1.658
- FOS of the outer shear failure surface 1.527
- FOS of the basal shear failure surface 1.291
- FOS of the slope 1.398

From the calculated FOS value it can be seen that the slope stability safety factor increases with further reduction of the slope angle. The reason for this is that flattening the slope angle has the effect of increasing the passive block size while at the same time removing the possible active block formation further away from the slope toe. See Figure 6.9 and compare it with Figure 6.8.

The slope failures in pit A-1 are very challenging to predict in terms of the newly proposed thrust failure mechanism, and at the same time very difficult to analyse with the aid of the well-known limit equilibrium methods. In the first place, both failures appeared in the same area. This means that in two failures we deal with identical rock properties and geotechnical conditions. Secondly, on the basis of the methods of slices the failures are very difficult to explain; why does a major collapse occur (as an event much bigger than the initial failure – see Figure 1.4) after an initial failure, which made the slope angle 5^0 flatter? The verification of the newly proposed thrust failure mechanism lies in the successful analysis of the failures and the mechanism's ability to give reasonable answers to the above question.

6.4 DISCUSSION

In general, the widely used limit equilibrium methods based on slices were created to fulfil the stability needs of earth dam walls, where the structure is relatively homogeneous, which is not the case with slope profiles in the mining industry. Figure 1.2 clearly shows all failure modes in open pit mining and consequently our success to prevent or predict them in practice. As a general weakness of the all known slope stability methods is that they cannot distinguish between natural and artificial slope profiles, where stress redistribution takes place in the strata.

In Chapter 3 we calculated the stress difference between the virgin and resultant stress state in the slope profile, which is actually the difference between the two slope types (natural and artificial). This difference, and particularly the stress component normal to sedimentation ($\Delta\sigma_N$), does not exist in the natural slope profile. For the sake of accuracy, it needs to be said that with time this difference diminishes (dissipates in deformation or fracturing), but this problem is then related more to time-dependent rock behaviour. In the same chapter we calculated the stress difference normal to sedimentation along the basal failure surface, which is tensile. It was interesting to see that the value of $\Delta\sigma_N$ increases with the flattening of the slope angle.

Bieniawski (1967) and Hoek and Bieniawski (1965) suggested that the weakest minerals in the rock matrix could be involved in tensile fracture propagation in low-porosity rock. In Chapter 4 was shown that carbon

flakes in the matrix of the shale layer are most susceptible to the remote tensile stress and could be used as an initial flaw in fracture initiation. This model is based on the Dugdale-Barenblatt analysis (Dugdale, 1960; Barenblatt, 1962) of a cohesive strip model. The Dugdale-Barenblatt model was extended to a periodic row of flaws, corresponding to the observed distribution of carbon flakes in the shale. In the chapter, the critical tensile stress ($\Delta\sigma_N^P$) for the specific embedded shale layer was calculated. We defined the fracture-process zone length as a major element in the $\Delta\sigma_N^P$ calculation. This zone length determines the $\Delta\sigma_N^P$ magnitude and the author's suggestion is that it should be used as a rock property.

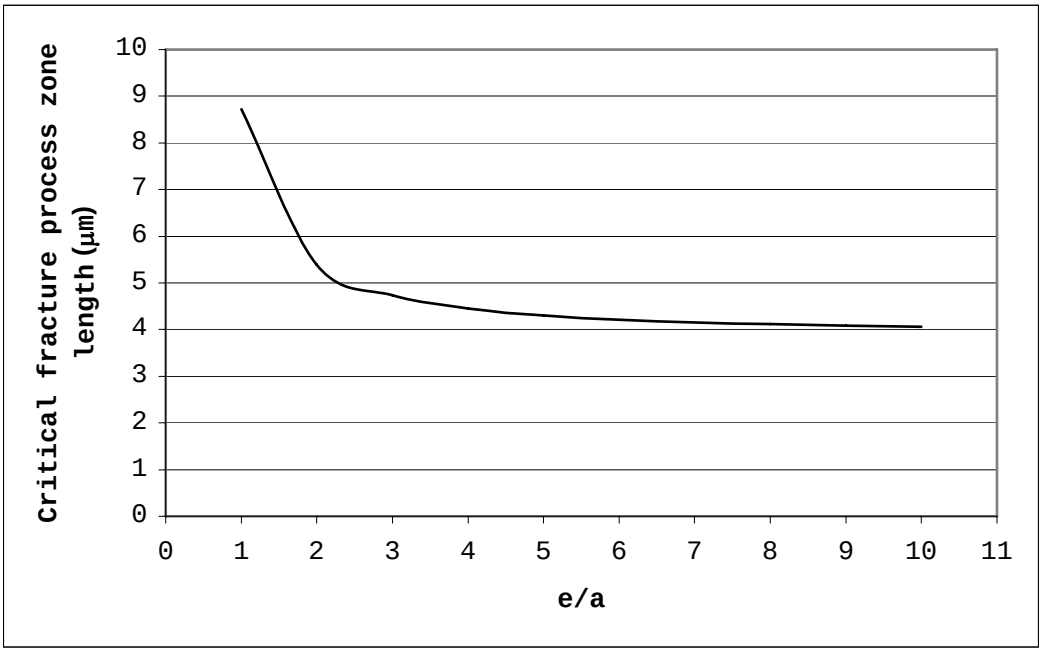

Figure 6.12

Dependence of the critical fracture process zone length (l_c) on a dimensionless coefficient; distance between flakes over half flake length (e/a)

Figure 6.12 shows the relationship (after Equation 4.20) between the critical fracture process zone length (l_c) and a dimensionless coefficient of the distance between flakes (e) and a half flake length (a). In the figure, the critical fracture-process zone length is proportional to the distance between two neighbouring flakes and inversely proportional to the flake length. We can also see that these parameters have a very strong relationship if the distance between neighbouring flakes is shorter than the flake length, and very weak relationship if this distance is longer.

For practical purposes it is more interesting to see the influence of these three parameters on the critical tensile stress value, $\Delta\sigma_N^P$. For this purpose let us use Equation 4.25 (as well as Equation 4.29) where $\Delta\sigma_N^P$ is proportional to the coefficient $\boldsymbol{arccos}\dfrac{\boldsymbol{sin}(\pi a/w)}{\boldsymbol{sin}[\pi(a+l_c)/W]}$. Further calculations show that this coefficient and consequently $\Delta\sigma_N^P$ drop only 0.3% when e/a increases 10 times. This is another confirmation for the constant value of the critical tensile stress ($\Delta\sigma_N^P$) in rocks.

To be sufficiently accurate at this point we should also discuss the influence of the shear stress on the failure process. Owing rock fracture mechanics, if we have shear stress and appropriate stress concentrators (in our case, carbon flakes), we should have conditions for mode II (shear) fracture propagation. Whittaker et al. (1992) discussed the critical fracture toughness coefficient of mode II (K_{IIC}), which is related to the mode I fracture toughness coefficient (K_{IIC} = 0.866K_{IC}). According to the laboratory test results, the shear

strength of most of the embedded weak layers (i.e. shale, siltstone or mudstone) is 25-30% higher than the rocks tensile strength results. Hence, according to the superimposed principle for mixed Mode I-II failure, we have a critical fracture process zone length as a result of the combined action of the remote applied stresses (tensile and shear). Following our Equation 4.20, by analogy we can say that the critical fracture process zone as a result of mode II loading will be shorter than the fracture process zone length as a result of relaxation. Hence for the simplicity of the calculations only the critical fracture process zone length was used in the thesis.

Of course this is not a general rule of analysis. With an increase in the slope depth we have a change in the k-ratio and, consequently a different stress state. The author thinks that with the increase in depth, the role of the relaxation stress will decrease, with the increase of influence of the shear stress on the fracture propagation process. It seems that in shallow-depth cuts (30-40m) the failure is driven by the $\Delta\sigma_N$, not the absolute stress state itself. Then in shallow cuts, the stress across certain flakes must still be compressive after the slope has been cut, even though there is a tensile stress ($\Delta\sigma_N$) that has been superimposed on the virgin stress state as an average value, coming from the continuity of the model. Stress deviation from the average value will occur because of the inhomogeneity of rock.

The new slope stability model is introduced in Chapter 5. We have calculated the safety factors associated with the two slope failures discussed in Chapter 1.

Table 6.2 Minimal safety factors, calculated for the failures presented in Figures 1.5 and 1.8 (including pore-water pressure)

Failure type	Thrust failure mechanism	Ordinary	Bishop	Janbu	Morgenstern - Price	
					Moment	Force
Pit A-2						
Circular failure	-	2.434	2.649	2.354	2.572	2.569
Blocky failure	-	1.198	0.157	0.152	0.113	0.144
Upper contact with spoil	1.375	-	-	-	-	-
Bottom contact with spoil	0.777	-	-	-	-	-
Upper contact - no spoil	1.287	-	-	-	-	-
Bottom contact - no spoil	0.794	-	-	-	-	-
Pit A-1; Initial failure – circular type						
Circular failure	-	0.709	0.729	0.708	0.722	0.716
Blocky failure	-	0.738	0.733	0.715	0.103	0.104
Upper contact	1.062	-	-	-	-	-
Bottom contact	0.902	-	-	-	-	-
Pit A-1; Major collapse – blocky type						
Circular failure	-	1.506	1.516	1.507	1.513	1.509
Blocky failure	-	4.718	4.619	4.329	4.870	4.870
Upper contact	1.224	-	-	-	-	-
Bottom Contact	0.908	-	-	-	-	-

These safety factors, together with the safety factors calculated by some of the well-known equilibrium methods appear in Table 6.2.

The table presents the calculated safety factors of the slope failure that took place in pit A-2, with spoil material behind the slope crest. There is very good agreement between the calculated safety factors in terms of the different methods for circular-type failure, but they indicate stable conditions for a slope that failed (FOS is between 2.354 and 2.649). Calculated results for blocky-type failure are unacceptably low, with values of about 0.12. If we have such low safety factors of the slope profiles, then we definitely will have failure during the construction of the slope. Obviously, the safety factor calculation process for blocky-type failure using slices is interfered with by the external load application.

The safety factors presented in Table 6.2 correspond to the multi-stage failure that took place in pit A-1 where was no external loading behind the crest of the slope (i.e. no spoil pile). Again, we have very good agreement between the safety factors calculated by the different methods for circular failure. Safety factors for blocky-type failure have more realistic values than for the previous case of failure and are close to those for circular failure, with the exception of the Morgenstern-Price calculation. The safety factors suggest both circular and blocky failure, without providing any information on which failure mechanism is more likely. In reality, the initial failure was circular in type and was reported by SRK (1995). The proposed thrust failure mechanism indicates relatively

higher safety factors, (FOS=1.062 and FOS=0.902), along the upper and bottom contact surfaces respectively, compared to the circular safety factor (FOS=0.72), which shows that the initial failure was more likely to be circular.

The major collapse took place shortly after the cleaning operations following the circular-type failure. In Table 6.2 it can be seen that safety factors calculated by the limit equilibrium methods show a stable slope with safety factors of approximately 1.51 and 4.52 respectively for circular and blocky-type failure. Obviously, limit equilibrium methods, used for safety factor calculations, become inapplicable in cases characterized by complex geotechnical conditions such as inclined multi-layered slope profiles.

Figure 6.13 shows a plot of the average safety factors for the circular failure of the slope profiles from pit A-1 before the initial failure, before the major collapse, and of the profile after major collapse. The safety factors calculated by the proposed method along the upper and bottom contact surfaces of the embedded shale layer are also plotted. The figure shows that at the initial failure, the circular-failure type has a lower safety factor than the proposed method safety factor, and as a consequence, circular failure took place, as was observed in the field. The new slope profile after the cleaning operations has a higher safety factor for the circular type of failure in terms of the proposed method and, as a consequence, the major collapse took place as a blocky type of failure.

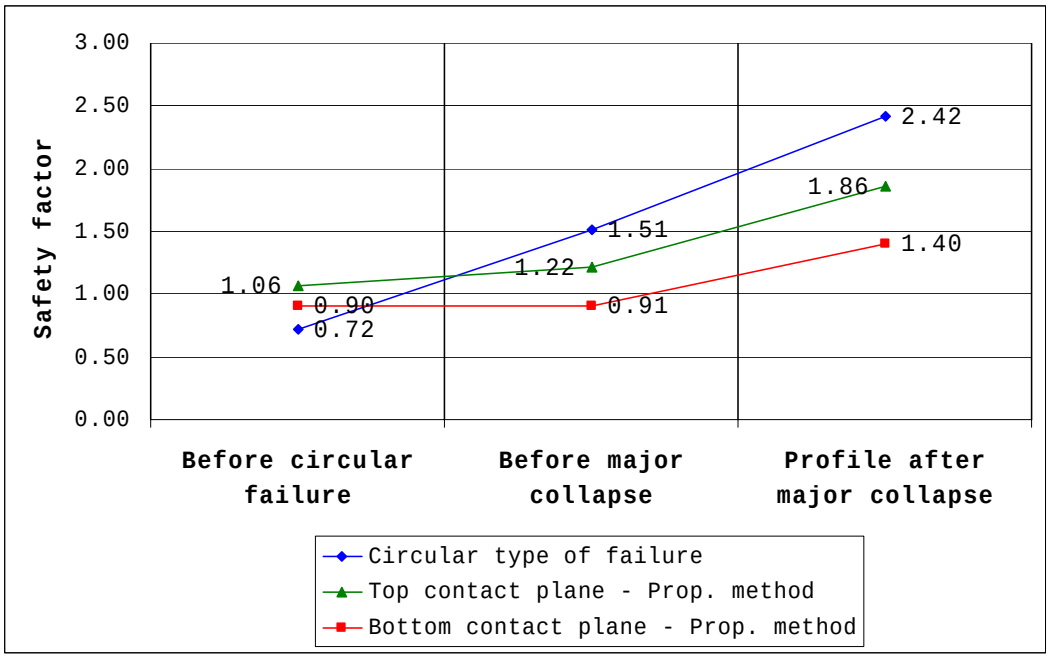

Figure 6.13

Plot of the average safety factors for circular-type failure and proposed method for blocky-type failure for the initial failure, major collapse and the profile after major collapse in pit A-1

The new slope profile (slope profile after major collapse - 10^0 flatter compared to the slope angle of the profile before major collapse) has safety factors indicating a stable slope profile and, in reality, there was no further failure. The other interesting feature, which can be seen on Figure 6.13, is the slope safety factors along the bottom contact surface. Here, despite the steeper slope angle of the profile before the initial collapse (55^0 slope angle), we have a relatively equal slope stability safety factor (0.902) to the slope angle of the profile before the major collapse (50^0 slope angle with FOS=0.909). In such situations there are clearly several conditions that have to be satisfied; e.g. dip angle, slope angle, cut depth and embedded layer thickness, which combination triggers the thrust failure mechanism.

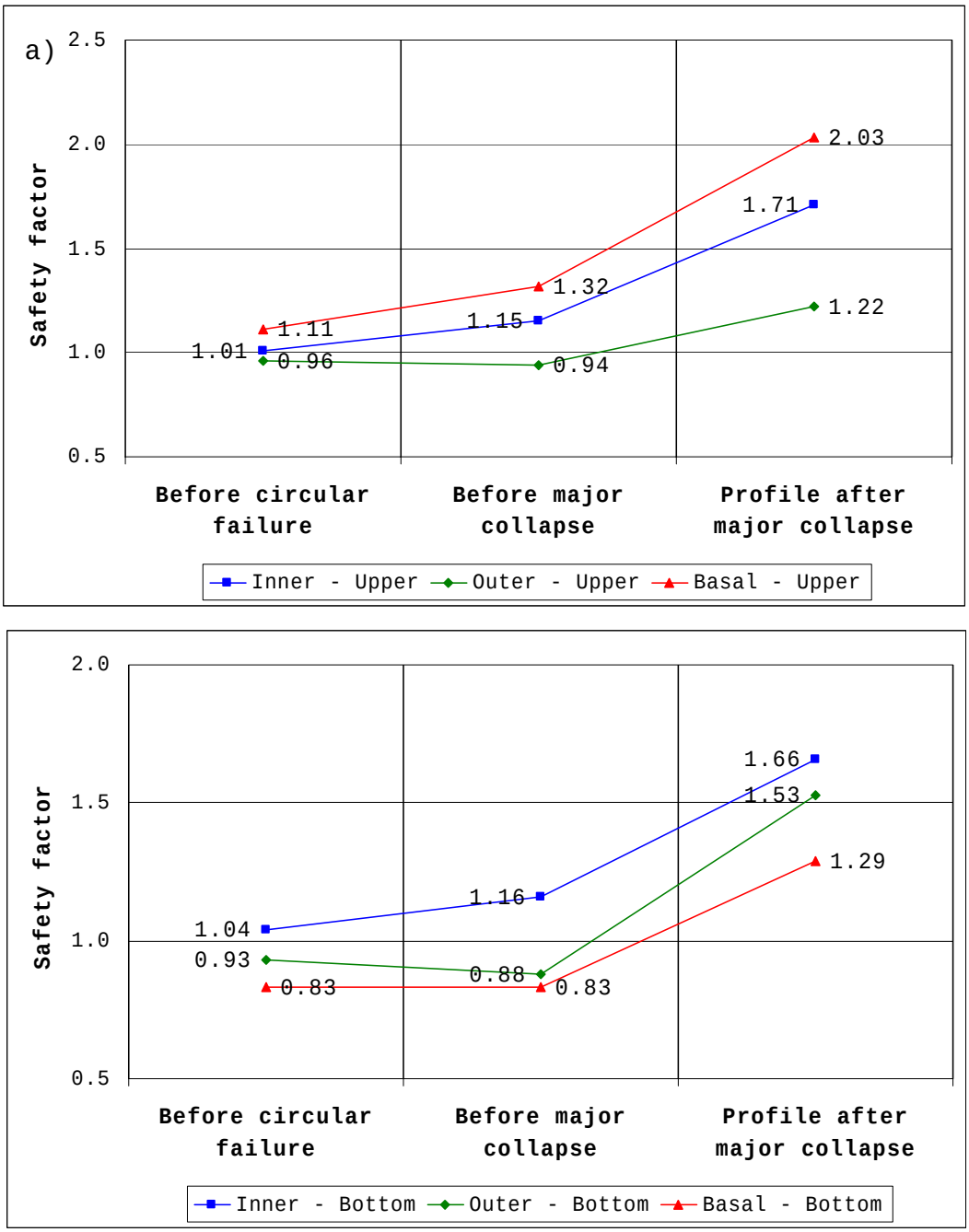

Figure 6.14

Plot of the safety factors on the separate shear failure surfaces of the proposed thrust failure mode for blocky-type failure along the: (a) upper contact surface; and (b) bottom contact surface before initial failure, major collapse and the profile after major collapse in Pit A-1

Figure 6.14 shows safety factors for the separate shear surfaces of failures along the top and bottom contact of the embedded shale layer. It can be seen that in all cases, the inner shear failure surface has a higher safety factor than the outer failure surface and follows the tendency of improvement of safety factors based on limit equilibrium methods in Figure 6.13. It is interesting to mention that the safety factor of the outer failure surface has almost constant value along the upper contact during the failure stages, while along the bottom contact surface the safety factor slightly decreases at the major collapse (FOS=0.88) compared to the initial failure (FOS=0.93). If we compare the calculated safety factors along the bottom contact surface (Figure 6.14b) before the initial failure with the safety factors before the major collapse, we will have confirmation for the specific conditions that triggered the thrust failure mechanism. In Figure 6.14b we have constant safety factor values along the bottom contact for initial failure and the major collapse. This means that initial failure does not improve the profile stability. Therefore, the safety factors along the contact surface has governing role for thrust failure mechanism.

Figure 6.15 shows the plot of the applied forces exerted by the separate blocks (active and passive) along the contact surfaces. Because of the lower depth, the applied load in the upper contact is lower than to the load on the bottom contact. The passive block load increases as a result of the increased length of the basal shear failure surface. Hence, the passive block load is proportional to the slope stability safety factor. This relationship can be used as an indication

that the proposed thrust failure mechanism could occur in deeper slopes with even a flat embedded weaker layer, such as a coal seam at the slope toe.

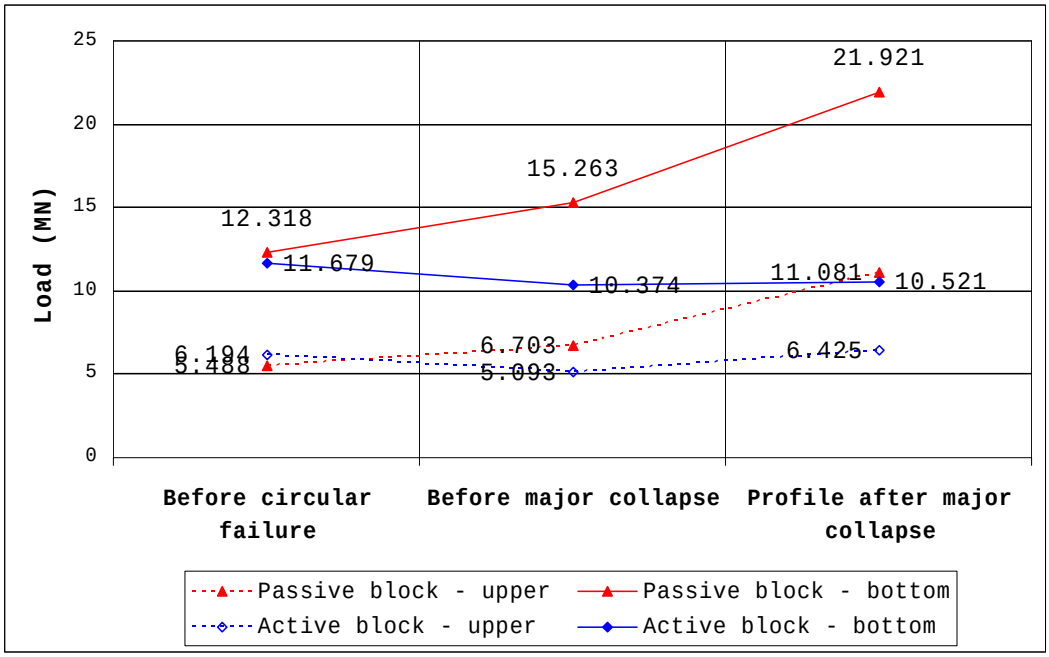

Figure 6.15

Force applied by the passive block (frictional plus cohesive zone) and the active block to the upper and bottom contact surfaces

The relationship of the blocks weight can be seen as a function of the contact surface inclination angle (bottom contact surface is always steeper than the upper). This relationship allows such failures to take place in shallow depths with steep contact surfaces for the embedded weaker layer.

Figure 6.16 presents the percentage of the frictional zone length in relation to the basal failure surface. It can be seen that before the initial failure we have frictional zone lengths of 86.5% and 83.3% from the potential failure surface in the passive block base along the upper and bottom contacts respectively.

Before the major collapse the frictional zone slightly increases to 87.2% and 86.7% along the upper and bottom contact surfaces respectively. In the profile after the major collapse, the frictional zone length along both surfaces drops to about 73%.

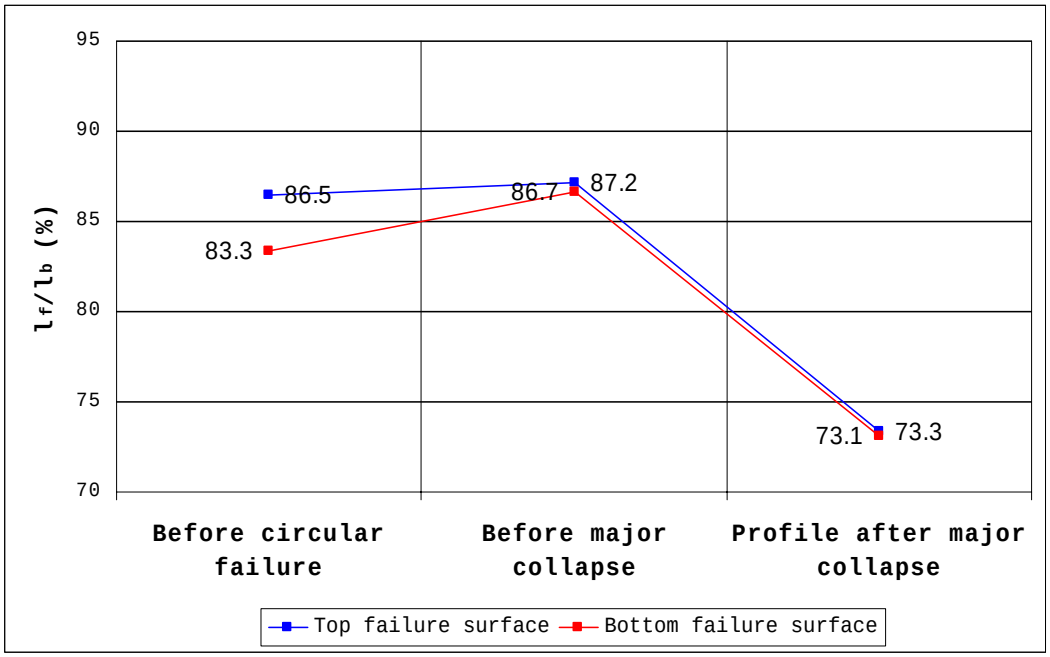

Figure 6.16

Percentage of the frictional zone length to the length of the basal failure surface (from the toe of the slope to the active block wedge)

This relation confirms again that slope failure is not a continuous process as a function of the slope angle flattening, but that there are conditions where the slope profile achieves stability. Surprisingly, in some conditions, the profile with the steeper slope angle is more stable than the profile with the flatter slope angle. Figures 4.10 and 4.11 also confirm where the profiles with a vertical slope angle have shorter frictional zone lengths than the profiles with a flatter slope angle. From Figure 6.16 it can be seen that along the bottom contact we have lower values for

the dimensionless coefficient l_f / l_b than for the upper contact. These findings mean that the upper contact surface of the embedded weak layer is more sensitive to the relaxation process than the layer's bottom contact surface but, because of the lower block weights, and flatter inclination angle we are less likely to have failure there compared to at the bottom contact.

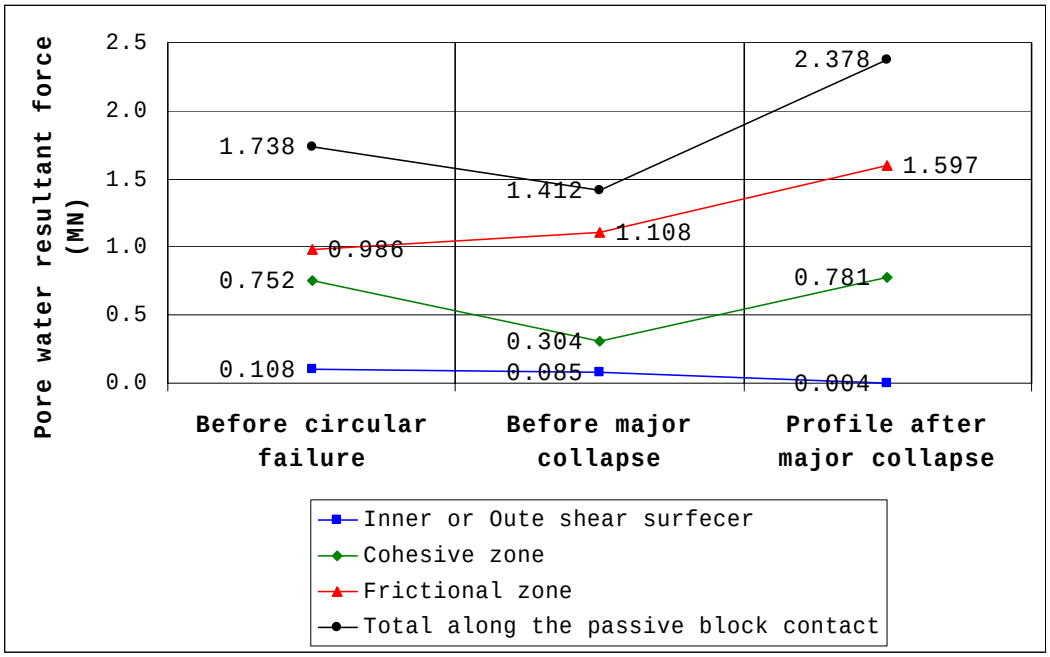

Figure 6.17

Resultant forces, created by the pore-water pressure and acting at the failure surfaces

Resultant forces, created by the pore-water pressure and acting at the failure surfaces, can be seen in Figure 6.17. As can be expected, the inner and outer sides of the active block shear surfaces have the lowest resultant force values, which is a function of their depth compared to the passive block shear surface (total length of the frictional and cohesive zones). In the figure, the lowest value of the pore-water pressure along the passive block contact is in the profile before the major collapse. It can clearly be seen that

before the major collapse we have the lowest value of the resultant pore-water force than for the other profiles. This low value can be explained by the fact that pore-water pressure is a function of depth and of length of the failed rock mass. In other words, the pore-water pressure is not the major factor that triggers the failure, because with the major failure we have the lowest pore-water pressure influence. Hence, we can indicate this as confirmation of the Stead and Scoble (1983) hypothesis that this failure mode is more stress related than the other geotechnical features are.

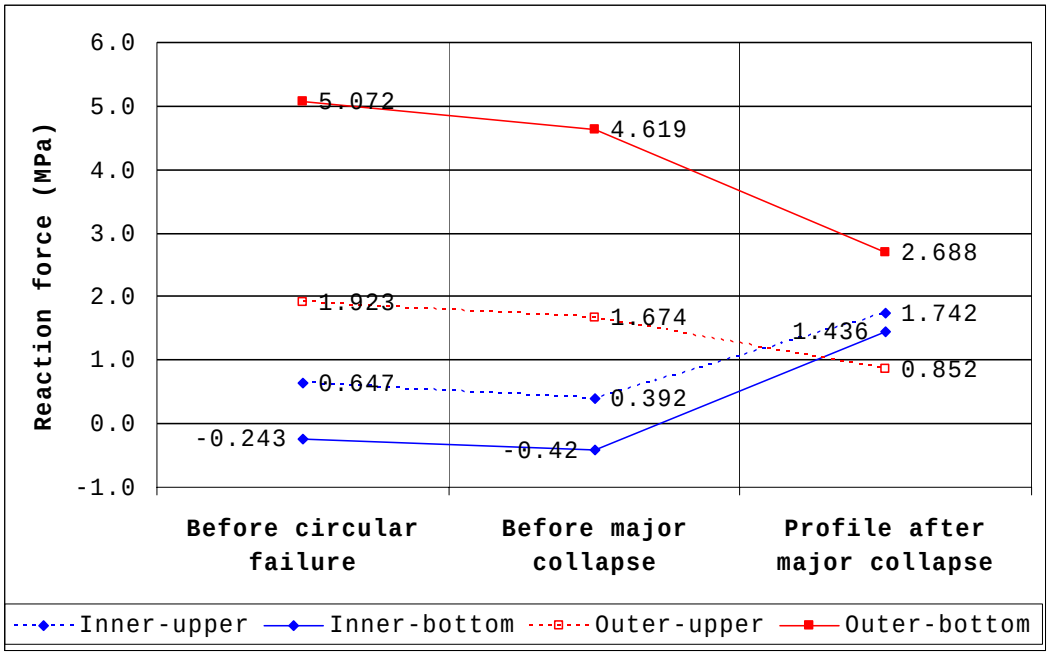

Figure 6.18

Reaction force of the passive block applied to the active block inner and outer shear failure surfaces

Figure 6.18 shows the variations in the passive block reaction force applied to the inner and outer shear failure planes. Their values are inversely proportional; with an increase of the reaction force applied to the inner shear failure surface, the

magnitude of the reaction force applied to the outer decreases. The negative value of the inner reaction force indicates a higher value for the driving forces than for the resisting forces along the basal failure surface. According to Equation 5.34, the negative value of the reaction force acting on the outer shear failure surface means an increase in the resisting forces along the outer shear failure surface. Such a case is apparent in the calculation of the safety factor on the upper contact of the profile after major collapse.

From Figure 6.18 it can be seen that along the upper embedded layer contact, we have an almost uniform reaction force acting on the inner shear failure surface and, respectively, an almost uniform reaction force at the outer shear surface of the profiles before the initial failure and major collapse. This indicates that because of the flatter contact surface, the passive block does not change in volume dramatically. Along the bottom contact surface of the profile before the major collapse we have an increase in the driving forces (see also Figure 6.16), which increase the negative value of the reaction forces along the inner shear surface.

On the other hand, in many slope profiles with developed relaxation cracks parallel to sedimentation, we do not have tensile fractures and stable slope profiles. Therefore, the sequence of fracture development depends on the material anisotropy and the calculated stress state of the profile. If the slopes were homogeneous and isotropic, then we could say that the tensile fractures at the frictional zone in the toe of the slope and the vertical tensile fractures behind

the crest of the slope are developed simultaneously. In the case of an inhomogeneous slope profile with anisotropic rock properties it is very difficult to indicate the right sequence of the tensile fracture appearance. Let us accept the ideal case, which in slope stability terms is the worst case, where the fractures propagate simultaneously. Hence, for the starting point we have two types of tensile fractures, propagated in the slope profile: one - in the bottom contact from the toe of the slope toward the solid; and two – vertical tensile fractures at the slope crest and some distance behind the slope crest (Figure 6.19a). After the formation of these fractures, the author accepts that the slope profile has relaxed and any further failures are the result of dead rock weight. As a result of the surface vertical tensile fracture formation, we do not have horizontal stress between them.

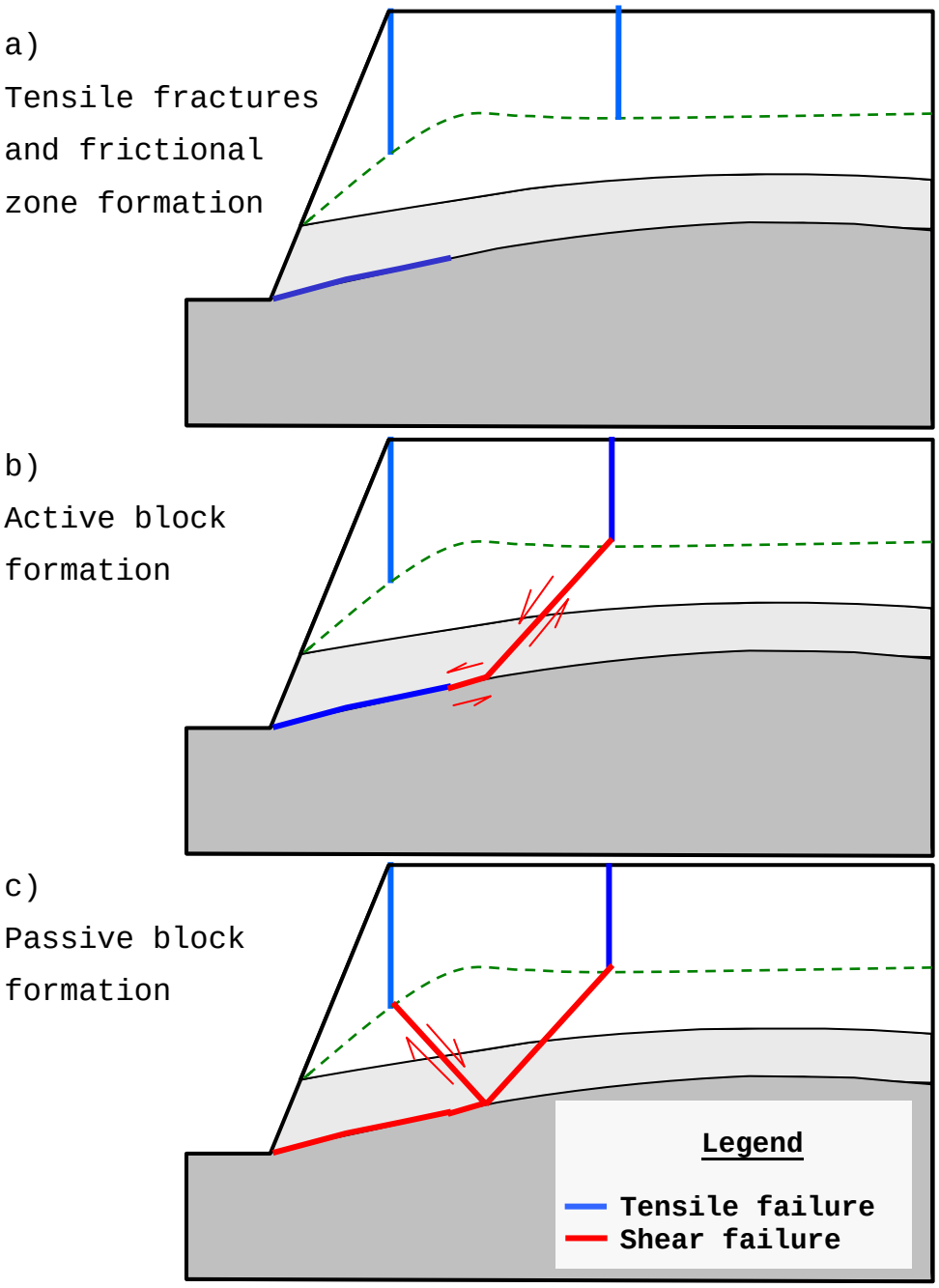

Figure 6.19

Failure sequence of the proposed thrust failure mechanism: a) tensile fracture formation in the slope profile due to stress relaxation; b) shear failure in the contact and inner shear failure surfaces forming the passive block (if we have the necessary conditions as discussed in Chapter 5); c) shear failure in the outer shear failure surface and formation of the active block

The way the shear fracture approaches a joint surface (similar to our frictional zone) in nature is shown in Picture 6.1.

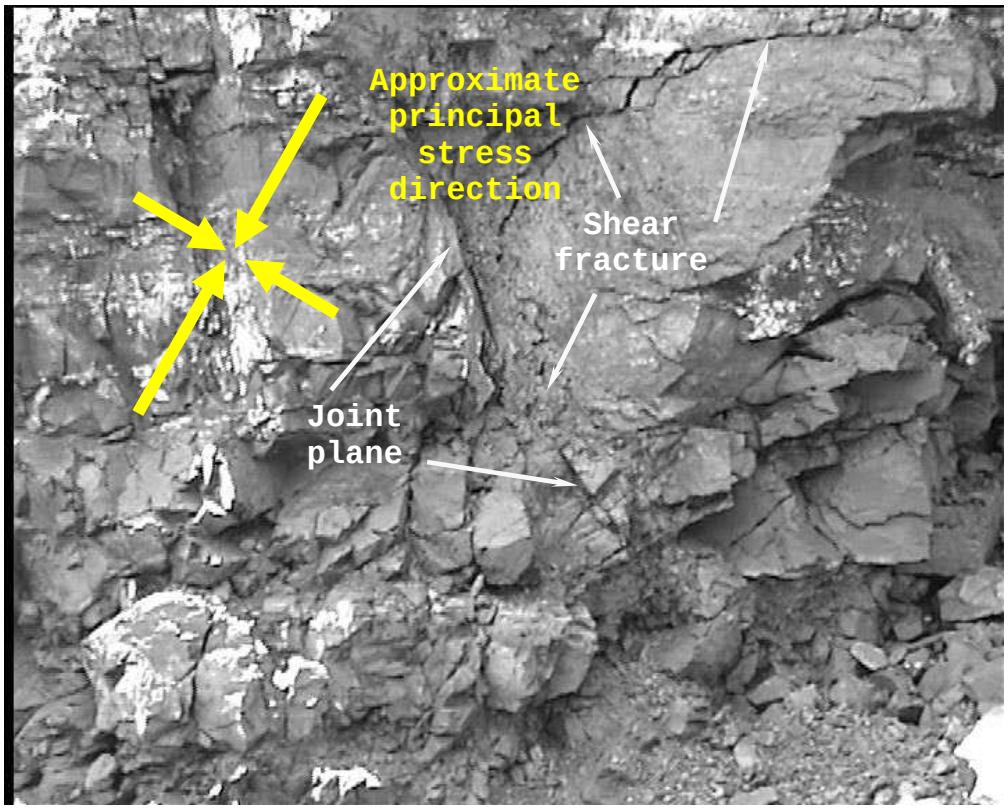

Picture 6.1

Way a shear fracture approaches the pre-existing joint plane

The next step in the slope failure is the shear fracture propagation in the cohesive zone along the bottom contact surface and along the outer shear failure surface (Figure 6.19b).

If we consider the fracture propagation type along the outer shear failure surface, it should strictly be a combination of tensile and shear modes (Atkinson, 1987). This means that the controlling failure parameter will be combined-mode fracture propagation, between Modes I and II, or so-called “Mode I-II”. The

tensile part of the failure Mode I-II is created by the material relaxation and the dip angle of the strata. It can be seen that this failure mode has two boundaries: the first is in the profile with flat layers, where we will have pure shear failure (Mode II), and the second in the profile with almost vertical layers, where we will have pure tension (Mode I). In Mode I-II failure, the outer failure surface should have a straight surface, in the case of the profile with flat layers, and a curved surface in the case of profile with almost vertical layers. Hence, in our discussed failure mechanism it is more likely to have the form of a "stepped ellipse" as can be seen in Picture 6.1, which shows a combination of Mode I and Mode II fracturing. For simplicity of calculation, in the proposed thrust failure mechanism, the author accepts a straight inner shear failure surface based on the relatively low strata dip angle, although this is almost always certainly not the case in actual failures.

The inner shear failure surface will lag behind the inner shear surface if we have the conditions for its creation, as discussed in Chapter 5. This failure surface is less influenced by the rock deadweight, experiences lower tensile stress and, as a consequence, a more planar surface forms compared to that for the outer surface (Figure 6.19c). The other feature that contributes to the inner shear failure surface is the contact undulation. If we have variations in the dip angle of the contact we will have conditions for the creation of more than one inner shear surface. See Figures 1.7 and 1.8.

Once the inner failure surface is formed, the thrust failure mechanism can take place. The active block sags under its own weight, forcing the passive block into the pit. The slightly later formation of the outer shear failure surface, compared to the inner, accelerates the passive block horizontal displacement. This mechanism accounts for all the features observed in the pit failures and those reported by Boyd (1983).

The other key factor in slope stability analysis is related to the pore-water pressure in the strata. The proposed thrust failure mechanism uses an approximation of the pore-water pressure as proportional to the depth. Because of the sandy overburden, the phreatic surface is relatively deep (23-25m) compared to the entire slope height (approximately 40m). For this reason we can say that the pore-water pressure influence on the slope stability calculations is insignificant. This statement is confirmed by the results of the slope stability safety factors, calculated along the shale layer bottom contact surface. After eliminating the pore-water pressure application we have a strengthening of the slope profile before initial failure by 5% (up to FOS=0.95), slope profile before major collapse by 9% (up to FOS=0.98) and the post-major collapse profile by 1% (up to FOS=1.46) compared to the calculated FOS values in Figure 6.13. These calculated differences confirm the low pore-water pressure influence on the slope stability analysis at shallow depths (30-50m).

The applied pore-water pressure approximation used in this thesis requires that all pores in rock are connected, which is not the case in nature and

especially not in the low-porosity rock considered in the failures discussed in this thesis. However, if tensile cracks form relatively early in the slope life, they could fill with rainwater and increase the potential for the formation of the shear stresses and contact shear/tensile surface. This is an extremely complex question because not all pores are hydraulically connected in the rock and their connectivity should be addressed by an independent study.

6.5 PRACTICAL IMPLICATION OF THRUST FAILURE MECHANISM FOR ACTIVE MINING SLOPES

The proposed thrust failure mechanism is a fast and easy method for slope stability assessment in complex geotechnical conditions, including strata inclined toward the pit that contain a weaker embedded layer exposed at the toe of the slope. Geotechnical engineers able to use this failure mechanism as a possible failure mode should first do the following:

1. Define weakest embedded layer at the toe of the slope profile
2. Calculate the critical tensile stress difference for the defined layer.
3. Calculate the cohesive zone length at the base of the passive block for a range of strata inclination angles appropriate for the slope under study.

As soon as this information is obtained, the proposed methodology can be used.

The assessment order for thrust failure mechanism can be seen in Figure 6.20 below.

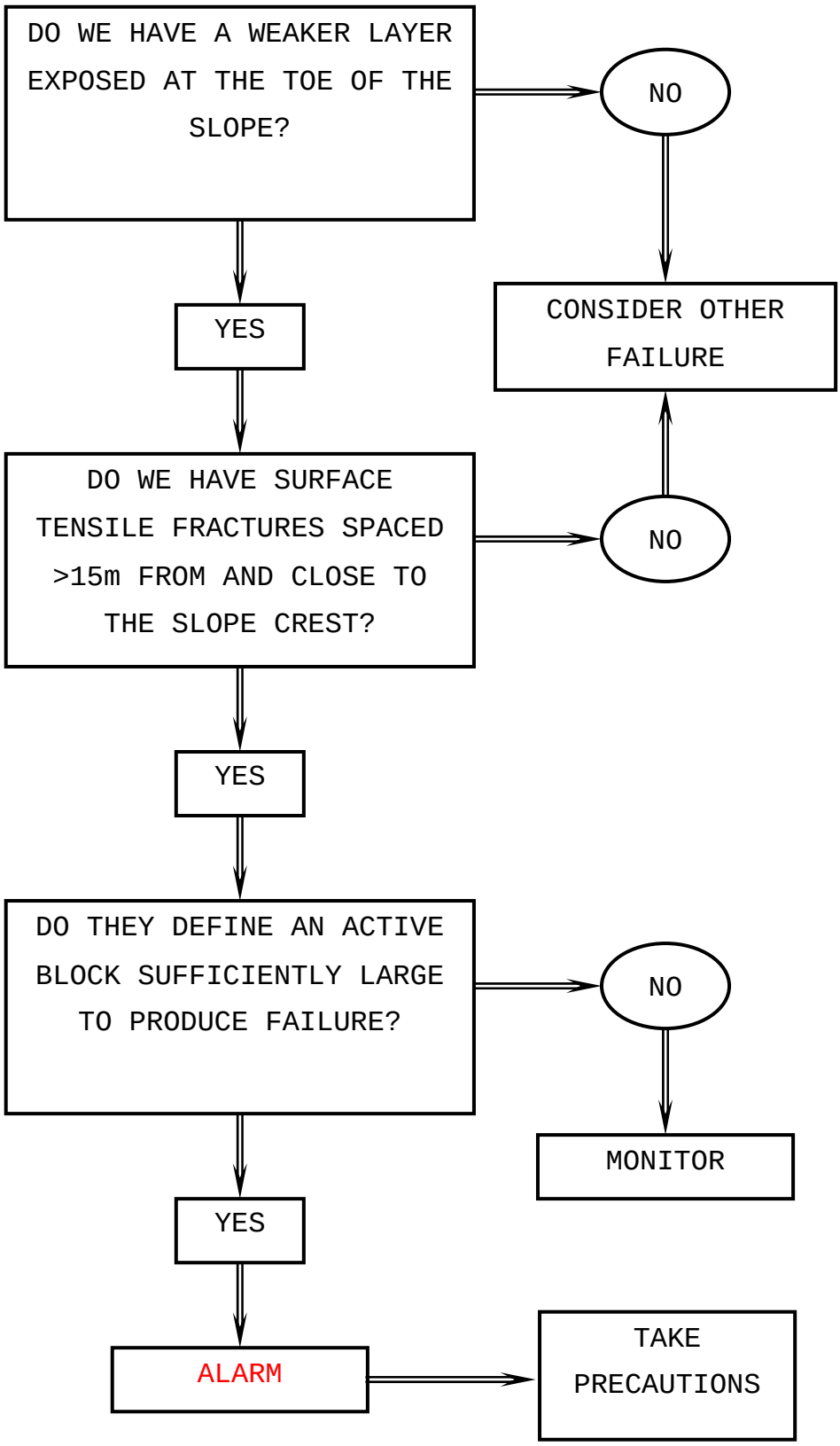

Figure 6.20

Assessment order for thrust failure mechanism

CHAPTER 7
CONCLUSIONS AND RECOMMENDATIONS FOR FUTURE WORK

7.1 CONCLUSIONS

The thrust failure mechanism, identified as a possible mechanism of failure of two slopes in a surface coal mine, shows good potential for use in slope stability analysis. The mechanism is based on a combination of observations at slope failure sites, numerical modelling data from models that account for the geology, micromechanical studies of tensile crack formation, application of the Mohr-Coulomb criterion and Riedel shear structures in the development of shear zones in slopes, and a crude pore water model for the slope. These are combined to create factor of safety computations for the various components of rock material failure that result in a structure that is able to collapse into the pit.

The first phase contributing to eventual slope failure is tension crack formation because of the relaxation of horizontal stresses near the pit edge: tensile cracks are commonly noted features at the crests of all pit slopes. This is followed by tensile crack propagation along the contact surface between (in this case) a shale and an underlying coal seam. Microscope studies revealed carbon flakes aligned with sedimentation in the shale, which would promote the formation of a tensile crack along the shale-coal contact because of the relaxation of vertical stress when the slope was cut. The detailed mechanism of crack formation was not confirmed in this study because the failure surface

becomes a slip surface for the collapsing slope. Once the slip surfaces were exposed at the mine, slickensiding and other slip features masked any evidence of fracture formation mode. The exact detail of fracture formation is not important, it is important that it formed a slip surface, which allowed slope collapse.

The formation of an active thrust block is completed by the development of two shear zones, which propagate from the deepest extent of two vertical surface tension cracks, dipping at 45° towards each other, to form a wedge facing downwards. These shear zones are postulated to meet at the level of the shale-coal contact, although there is no physical reason why they have to meet there. Once the active thrust block has formed, it tends to subside under its own weight, which will force the further growth of the tensile crack already formed along part of the shale-coal contact. This further growth is probably mixed-mode I-II growth. Once the mixed-mode crack has reached the base of the active block wedge, the entire slope stability is dependent on frictional forces alone. If friction is insufficient to maintain stability, the active block will slide downwards under its own dead weight, thrusting the passive block into the excavation.

The thrust failure mechanism of slope failures appears to be a more accurate model compared to the limit equilibrium methods for slope failures in complex geotechnical conditions. The limit equilibrium methods were created to account for failures mainly of earth dam walls and homogeneous soil slopes. The circular failure mode was shown in one slope failure to be a

reliable predictor of failure in such conditions where failure only involves homogeneous sandy overburden.

The following specific conclusions can be drawn:

1. The thrust failure mechanism takes into account the virgin and resultant stress state of the profile along a contact surface involved in frictional zone formation.
2. The proposed mechanism takes into account the rock anisotropy at a micromechanical level, and minerals or pores in the rock, which provide insight into the probable fracturing process.
3. The new failure mechanism takes into account the critical stress for fracture propagation, which is a function of the flaw size and inter-flaw distance.
4. The new failure mechanism defines two zones along the slip surface: frictional and cohesive. In the frictional zone resisting forces are formed only by the normal load and frictional coefficient, while in the cohesive zone, the cohesive rock strength is also included.
5. The critical stress magnitude defines the frictional zone length of the slip surface, which is a vital parameter for frictional-type failure type along the surface.
6. A fracture mechanics approach is not appropriate to determine the potential for the development of a frictional zone in the slope; it does provide some useful guidelines.
7. Since fracture mechanics analyses failure from a stress point of view will not help uncover the actual mechanism of crack development on the shale-

middle coal seam contact, a strain based approach may yield better results.

8. With the aid of this method a more realistic slope stability safety factor and appropriate general slope angle are possible.
9. Pore-water pressure influence in slope stability analysis using the thrust failure mechanism is highly dependent on the strata and could be insignificant in shallow cuts (30-50m deep).
10. Although fracture mechanics were used, this work does not attempt to derive a realistic damage model or fracture-propagation model for either the tensile or shear segments of fractures.
11. The proposed thrust failure mechanism uses the Riedel (1929) shear structure model for shear zone orientation in the slope.
12. This study is merely a practical study of evaluating the potential for the block thrust failure mechanism to take place, and the safety factor derived for two observed failures in the field appear to be reasonably accurate.
13. The further application on the proposed thrust failure mechanism in slope failures could indicate some possible weak points and increase the accuracy of the method.

The objectives of this study are to explain the mechanism of slope failure in complex geotechnical conditions, and to find a simple and practical way to evaluate the potential for slope failure in a practical mining situation. The block thrust mechanism proposed here meets both objectives above, but will require wider application before its value as a slope stability indicator can be established.

7.2 FUTURE WORK

Future work should include the influence of pore-water pressure in the proposed method for blocky-type failure using the linear porosity theory. Encouragement for the success of the work is based on the work done by Wong et al. (2001a and 2001b) and Mandal et al. (2001). The linear porosity theory was not applied in the thesis because the embedded shale layer is rock with very low porosity and, as was mentioned earlier, the fracture initiates from the carbon flakes. In other rock types, sandstone for example, fractures initiate from the pores in the rock matrix (El Bied et al., 2002). For this purpose, the linear porosity has to be used for the pore size measurements. The work done by Olson (1993 and 1997) and Olson and Pollard (1989) regarding natural fracture propagation and the influence of the pore-water pressure promises to be successful. The author's opinion is that including the pore water pressure, using linear porosity theory, will further decrease the values of the pore-water forces applied along the failure surfaces. As a result, the defined shear failure surface safety factors are expected to be slightly higher.

The critical length of the fracture-process zone between carbon flakes needs further confirmation. The length of the fracture-process zone is one of the most important parameters, which could be used even as a rock property, because this value is used directly in the critical tensile stress calculation. Alternatively, a future research should follow strain-

based approach, as this is more likely to yield acceptable results.

The distance between surface tensile cracks is a third important area of study. The fracture mechanics analysis made by Parker (1999), Bai and Pollard (2000a and 2000b) show that the minimal distance between two tensile fractures should be equal to their length. On the basis of this development, the horizontal distance between the surface tensile fractures involved in active block formation must be at least equal to their depth. Hence, the failure along the upper contact plane at shallow cuts (with depth less than 30m) will not develop because the active block width is too small, resulting in its weight being too low to allow the thrust failure mechanism to work.

The Riedel (1929) shear failure model is virtually unknown in rock mechanics, yet it is widely used in structural geology. Combining Riedel's (1929) findings in shear failure structure with the modern fracture mechanics using a strain-based approach could shed more light on the complexities of shear zone formation and failure. Final confirmation of the block thrust failure mechanism will only come with the confirmation of fracture processes within slopes.